Modeling a MOCVD process to apply alumina films on the inner surface of bottles

P.-L. Etchepare [a,*], H. Vergnes [b], D. Samélor [a], D. Sadowski [a], B. Caussat [b], C. Vahlas [a]

[a] Centre Interuniversitaire de Recherche et d'Ingénierie des Matériaux (CIRIMAT), ENSIACET, 4 Allée Emile Monso, BP 44362, 31432 Toulouse Cedex 4, France
[b] Laboratoire de Génie Chimique (LGC), ENSIACET, 4 Allée Emile Monso, BP 84234, 31432 Toulouse Cedex 4, France

A B S T R A C T

Deposition inside a cavity with a narrow neck, i.e. a hollow body, is a challenge, in particular for the supply and the evacuation of the reactive phase and of the effluents through the same entrance. High gradients (pressure, velocity, species concentrations) and important convective mechanisms related to the impacting jet of the gaseous phase on the bottom inner wall of the cavity are created in that region. Given the increasing number of experimental parameters, modeling helps efficient process optimization with better understanding of physical and chemical phenomena occurring inside the hollow body. This study presents a numerical modeling using the CFD code Fluent to simulate a direct liquid injection metalorganic chemical vapor deposition of amorphous alumina coatings from aluminum tri-isopropoxide (ATI) on the inner walls of a glass bottle. The model is used to predict local profiles of gas velocity, temperature and species concentrations into the reactor as well as local growth rate based on an apparent heterogeneous kinetic law of ATI decomposition. Comparison with experimental thickness profiles allows validating the model and leads to a better insight in the phenomena which impact film thickness inhomogeneity along the inner surface. The model contributes to the improvement of the reactor configuration by increasing the distance between nozzle and bottle and the outlet section of the nozzle.

1. Introduction

Chemical vapor deposition (CVD) allows the application of a coating on a heated part, by the transport in the reaction chamber and the decomposition on the surface to be coated, of a gaseous reactive molecule. CVD processes are of industrial interest offering a variety of coating types and compositions and answering severe technological specifications, such as conformal coating of complex surfaces with high growth rate. However this process is subjected to a strong interplay between fluid flow, thermal profile and often complex chemical mechanisms both in the gas phase and on the growing surface. Consequently, it is difficult to understand and to predict the underlying transport phenomena and deposition mechanisms [1]. When high uniformity is requested, process modeling is a valuable tool as was illustrated in the past with the modeling of silicon CVD [2–4]. The mathematical models were used to describe both homogeneous and heterogeneous reaction mechanisms from silane SiH_4 at low pressure and to simulate transport phenomena and silicon growth rate. Computational Fluid Dynamics (CFD) models of CVD reactors are useful for process optimization [5]. Chemical mechanisms and kinetic schemes have been investigated for a variety of such processes. Determination of gas flow, temperature, and deposition rate profiles into the deposition chamber provides insight into numerous complex phenomena that cannot be easily solved by intuitive and tedious approach with trial-to-error development. Kleijn [6] used a model to differentiate kinetic and transport effects and analyzed the impact of precursor flow rate and reactor geometry on the difference of coating thickness between depth and width lengths of a micronic trench for the CVD of tungsten. Chae et al. [5] extracted the deposition kinetic law from small-scale experiments and reported the influence of the showerhead-to-wafer distance and of the position and dimensions of the outlet to control the film thickness uniformity for tungsten silicide deposition in the temperature range 130–360 °C under 400 Pa.

To overcome drawbacks of thermal incompatibility with the substrate and risks of manipulations of corrosive effluents, CVD from liquid or solid metal-organic precursors (MOCVD) is often performed at relatively low temperature. Composition, nature of deposited phases, stoichiometry, crystallinity and microstructure of the material can be adjusted by finely tuning MOCVD operating parameters among which the nature and composition of the input gas phase. However, in this case the situation becomes more complex due to the complicated decomposition mechanisms of thermally sensitive molecular compounds in the gas phase and on the growing surface. This chemistry is often hard to catch due to the difficulty to implement non-intrusive metrology for the in situ monitoring of the process. Despite these difficulties, Xenidou et al. [7] recently modeled the deposition of aluminum on flat substrates from dimethylethylamine alane injected through a showerhead in a vertical cold-wall reactor. They revealed the influence of deposition temperature on the deposition rate profiles of aluminum and highlighted a phenomenon of gas recirculation inside the showerhead.

* Corresponding author.
E-mail address: pierreluc.etchepare@ensiacet.fr (P.-L. Etchepare).

In another study the same authors' analysis of the interplay between reaction and transport phenomena, allowed improving the process by tuning the growth temperature, the distance between the showerhead and the substrate, and the geometry of the gas delivery system [8]. The MOCVD of alumina from aluminum tri-isopropoxide ($C_9H_{21}O_3Al$, ATI) has been modeled by Vergnes et al. [9]. The authors established an apparent kinetic law of the heterogeneous decomposition of ATI into stoichiometric alumina. The kinetic parameters were fitted from experimental data, obtained from dedicated deposition experiments performed in a hot-wall horizontal reactor at 666 Pa between 360 °C and 496 °C. Then, a 3D CFD-model was created taking into account the kinetic law and the thermal profile of the reactor to simulate the alumina growth rate profile. A good agreement was found between calculated and experimental results which validated the model. The present work is based on the kinetic model proposed by these authors. Other kinetic schemes exist in the literature [10,11] but processing conditions are out of the range of interest for this study in terms of deposition pressure and temperature.

Gas phase deposition of thin films inside cavities or on the inner surface of closed geometry with a unique orifice has already been investigated [12–18]. Such processes require a particular attention to hydrodynamics inside the cavities. Interactions between inlet and outlet reactive flows at the often narrow entrance can be managed in some cases by introducing the feeding tube inside the part [12]. However, such a solution may be problematic for industrial implementation, and for this reason, maintain of the feeding equipment (e.g. gas injector) close but outside the part to be coated could be more sustainable.

Modeling of deposition into centimetric cavities requires a different approach than that in micrometric trenches which has long been studied, motivated by the microelectronics industry [1]. In such micrometric trenches, the precursor is not supplied by convective flux inside the cavities and the transport phenomena become ballistic because of high Knudsen number. To the best of the authors' knowledge, modeling of MOCVD process for the deposition on the inner surfaces of hollow bodies has never been attempted. This is the object of the present contribution, applied to the MOCVD of amorphous alumina (a-Al_2O_3) optically transparent films from ATI on the internal surface of glass bottles for anti-corrosion and alkali ion diffusion barrier multi-functionality. To meet this objective, we combine numerical simulations of the reactor and coating experiments.

Films composed of a-Al_2O_3 are selected for this purpose due to their excellent barrier and anti-corrosion properties [19–22] and high optical transmission [23]. They compete with silica based coatings which also present excellent barrier properties, although limited durability [24]. Considering the complex geometry of a bottle, the thickness uniformity is not a severe requirement provided that the film is thick enough to ensure the expected performance and thin enough for satisfactory adhesion to the glass surface. Such weak constraints in thickness uniformity are not exceptional. For example, Boutroy et al. deposited hydrogenated amorphous carbon films on the inner walls of PET bottles using a microwave plasma assisted CVD at very low pressure with a requirement about film thickness uniformity of $\pm 15\%$ [12].

ATI is one the most used precursors for the MOCVD of a-Al_2O_3, due to its low cost, to its single source nature (it does not require extra oxygen for the processing of stoichiometric alumina) and to its high volatility which ensures high growth rates, required for industrial implementation. The decomposition kinetics of ATI has already been investigated [25]. CVD regimes and film composition both depend in particular on the deposition temperature. The evolution of the growth rate versus deposition temperature is divided in two distinct parts, differing by both the deposition regime and the composition of the film. For a process operating at 5 Torr, with ATI vaporization by bubbling N_2 without reactive gas, the dominant reaction for films grown at temperatures lower than 415 °C leads to the formation of an hydroxylated phase $AlO_{1+x}(OH)_{1-2x}$ in which the amount of hydroxyl groups increases with decreasing temperature. In this domain, the growth rate significantly increases with increasing temperature witnessing a surface reaction limited regime. Amorphous stoichiometric Al_2O_3 is deposited for temperatures between 415 and 650 °C. For deposition temperatures higher than 650–700 °C, either crystalline nanoparticles of γ-Al_2O_3 appear in the amorphous matrix [26] and/or undesired homogeneous reactions occur [27]. The formation of such mixed microstructure with the presence of grain boundaries is harmful to the chemical durability [19] and the barrier properties of the thin film [20]. It is thus not conceivable to perform depositions at temperatures higher than 650–700 °C with the aim to increase the growth rate.

MOCVD of stoichiometric a-Al_2O_3 from ATI is potentially attractive because:

a. The 415–650 °C temperature range is wide enough to ensure a robust process;
b. Taking into account the low activation energy of 12 kJ/mol [25], processing in this temperature range results in mass transport limited operation. The evolution of growth rate by varying temperature is smooth and ensures process stability, taking into account the inhomogeneous temperature profile of the bottle (see hereafter).
c. a-Al_2O_3 films deposited from 415 to 650 °C present optimal mechanical and anti-corrosion properties [19]. This range corresponds to a maximum of the 4-fold coordinated aluminum sites ($^{[4]}$Al) and to a minimum of 6-fold coordinated ones ($^{[6]}$Al) in the film [28].

For these reasons, a temperature of 480 °C at the bottom of the bottle has been chosen generating thermal profiles along the height of the bottle ranging from 480 to 660 °C. The process provides films with smooth and dense microstructure in the temperature range 450 °C to 700 °C [26], and is well documented [9,20,25,27,29–33]. It is worth noting, however, that in all these works, ATI was vaporized and transported to the deposition chamber, from a bubbler. In the present contribution, a direct liquid injection (DLI) technology is used with the aim to ensure robust and reproducible transport of ATI dissolved in cyclohexane [34].

In that which follows, the experimental setup will be presented first, followed by the modeling procedure, involving the computational fluid dynamics (CFD) code Fluent. Then, the results will be presented and discussed, revealing the interest of such combined numerical and experimental approach prior to providing concluding remarks.

2. Experimental

Fig. 1 schematically presents the DLI-MOCVD setup. Deposition takes place in a vertical hot-wall reactor, composed of a quartz tube (5.5 cm in diameter and 33.5 cm in height), where the reaction zone is defined by an external, thermoregulated, inductively heated, coaxial stainless steel (SS) tube. The glass bottle to be coated (4.25 cm in diameter and 7.3 cm in height) is first cleaned in ultrasonic bath with acetone and ethanol and then positioned on a metallic support. Temperature is monitored by a thermocouple in contact with the external bottom surface on the central axis of the bottle. All experiments are performed at 480 °C at this point. The resulting thermal profile was experimentally determined by measurements with another thermocouple at different heights on the internal bottle walls in process conditions of Runs A, B and C, as shown in Fig. 2. These temperature profiles depend on the reactor configuration and in particular on the position of the bottle relatively to the inductively heated SS tube whose position remains unchanged. The thermal profile was then determined and fitted with a polynomial function written in a macro. We also measured gas temperature at several points along the central axis. We found a satisfactory agreement between the experimental gas temperatures and those calculated from the thermal profile imposed on the walls.

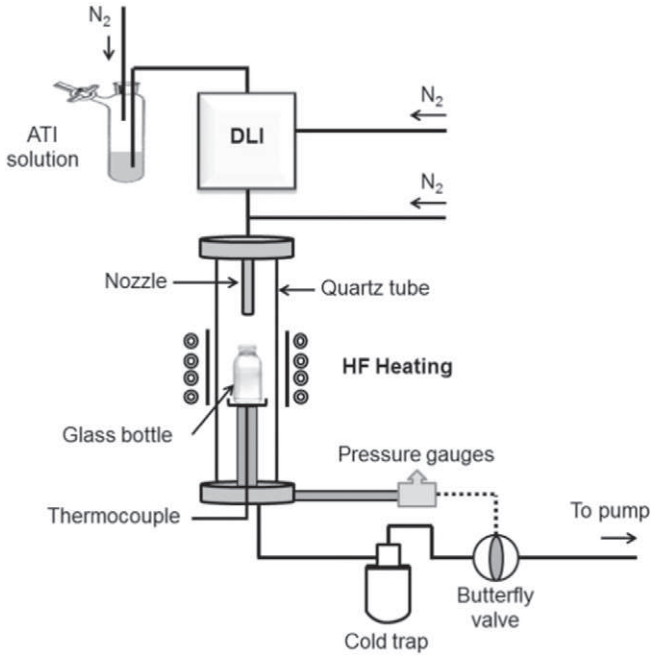

Fig. 1. Schematic of the DLI-MOCVD setup for the deposition of a-Al_2O_3 films inside the bottles.

ATI (98% pure, Acros Organics CAS N° 555-31-7) was used as precursor, dissolved in cyclohexane (99.5% extra dry, Acros Organics CAS N° 110-82-7). The solution was atomized and then totally vaporized at 200 °C in a Kemstream Vapbox 500® DLI equipment. This reactive gas phase was diluted with pure N_2 and introduced in the reactor at its upper part through a SS nozzle. The temperature of the nozzle was ca. 412 °C for Run A and 500 °C for Runs B and C (detailed hereafter), meaning that deposition of a-Al_2O_3 was initiated inside the nozzle. SS transport lines between the exit of the DLI and the inlet of the reactor were heated at 200 °C to prevent condensation. The total gas flow rate and the inlet ATI molar fraction were maintained unchanged at 585 standard cubic centimeters per minute (sccm), and 1.7 10^{-3}, respectively. A mass flow rate controller (MKS) was used to regulate the dilution flow of N_2. Total pressure was regulated at 666 Pa by a pressure gauge and a throttle valve (both MKS) positioned between the reactor and the pump. Gaseous by-products were condensed on the walls of a cold trap upstream the pump. Deposition duration was fixed at 30 min. Preliminary depositions were performed on 1 × 2 cm^2 silicon wafer coupons in the same operating conditions.

After deposition, the bottles were fractured following their vertical axis. The film thickness profile along the internal surface of each bottle was measured using cross-sectional scanning electron microscopy (SEM) performed on a LEO 435VP instrument. The elementary composition of the coating was investigated by Electron Probe Micro-Analysis using a Cameca SX50 instrument. X-ray Diffraction was performed on SEIFERT-3000TT to study the alumina phase.

3. Process modeling

The MOCVD reactor was simulated using the computer-aided design software, mesh generator and CFD code FLUENT 15 of the ANSYS suit. Taking into account the axial symmetry of the reactor, a half cross section in 2D configuration was considered. The grid was composed of structured meshes. Preliminary calculations were performed to verify grid independence of the results. The mesh was refined in regions close to the bottle walls in such a way that the mass boundary layer contains more than 10 cells and at the bottle inlet because high gradients of gas velocity were expected. Finally it was formed of 48,638 to 100,620 cells, depending on the reactor configuration.

Differential equations describing conservation of mass, momentum and energy, and gas species concentration including kinetics of alumina deposition were solved to calculate local profiles of gas flow, temperature, mass fraction and deposition rate inside the reactor. SIMPLE algorithm was used to calculate the solutions of the Navier–Stokes nonlinear equations with a first-order spatial discretization. Steady-state, ideal gas and laminar conditions (Reynold number lower than 525) were assumed. Compressibility effects were considered since the Mach number can be as high as 1.4. The equation of energy was calculated considering convective and conductive transport. Due to the low ATI molar concentration, the heat of reactions was assumed to be insignificant compared with the applied inductive heating and was not taken into account.

A kinetic model was implemented into the code to simulate the deposition of alumina from ATI. The following apparent chemical reaction

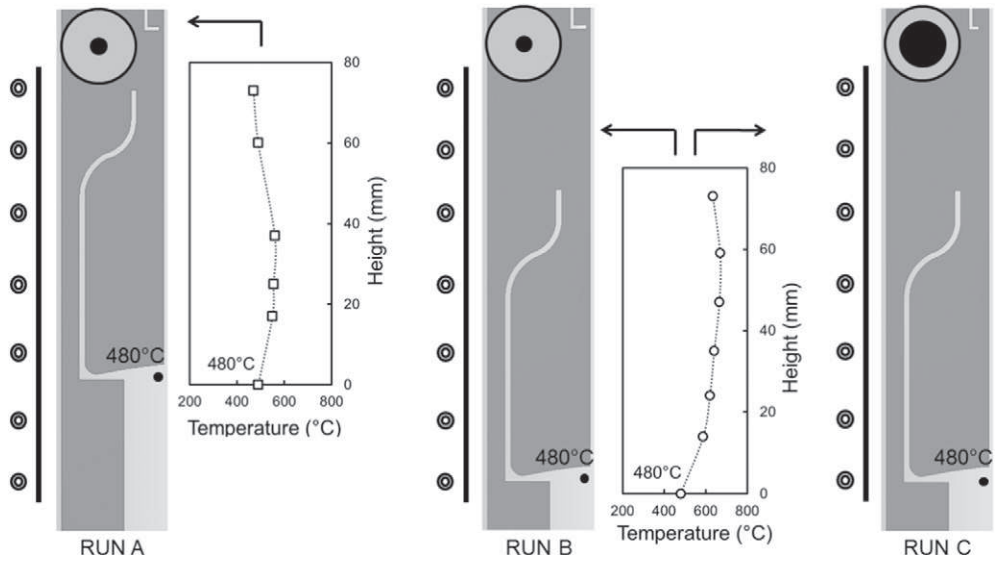

Fig. 2. Schematic illustrations of the reactor for Run A, Run B and Run C with relative positions among the bottle, the heating tube and the fixed nozzle, and associated experimentally determined thermal profiles where lines are guide to the eye. The circles on the top represent bottom views of the nozzle outlet with the feeding hole in black.

was defined, considering that ATI is tetramer both in the condensed and in the gas state [25]:

$$[Al(OC_3H_7)_3]_{4,g} \rightarrow 2Al_2O_{3,s} + 12C_3H_{6,g} + 6H_2O_{,g} \quad (1)$$

where subscripts g and s hold for gas and solid, respectively. Chemical reactions in the gaseous phase were not considered. The corresponding apparent heterogeneous kinetic law was defined by Hofman et al. [10]:

$$R_{si} = k_0 * \exp(-E_a/RT) * [ATI]^n \quad (2)$$

where R_{si} (kg/(m^{2}s)) is the growth rate, k_0 is a pre-exponential constant, E_a (J/mol) an activation energy, T (K) the temperature, [ATI] (mol/m^3) the ATI concentration and n the apparent reaction order. The kinetic parameters were taken from Vergnes et al. [9], as $k_0 =$ 5.81 10^7 kg·m$^{2.5}$/(mol$^{1.5}$ s), $E_a = 78.1$ kJ/mol and $n = 1.5$.

Properties of the gaseous species and the multicomponent diffusion coefficients were calculated using the kinetic theory of gases and the Chapman–Enskog theory, respectively. Lennard–Jones parameters for N_2 and H_2O were taken from the FLUENT database whereas those for C_6H_{12} and C_3H_6 were taken from Bird et al. [35]. These parameters are unknown for ATI and were considered to be the same as those of n-decane, this molecule having almost the same number of carbon atoms. The ATI molar fraction being low, a small error on these values does not affect the results of the simulations.

The inlet ATI and C_6H_{12} mass fractions, the total mass flow rate and the inlet gas temperature were taken equal to those ensured by the DLI system at the nozzle inlet. At the exit, the total pressure was fixed to the operating value. The experimentally measured thermal profile was fixed as thermal boundary conditions on the bottle and on the reactor walls rather than heat flux which is difficult to evaluate from the heating elements of the reactor. Mass flow density of each species on walls was assumed to be equal to the corresponding heterogeneous reaction rate. A classical no-slip condition was used on the walls for gas velocity.

4. Results and discussion

Preliminary depositions were performed on flat silicon coupons in conditions similar to those applied for the deposition in the bottles with the aim to analyze the composition, structure and morphology of the films and to investigate the effect of ATI molecules dissolved in a solvent. It appears that films are composed of stoichiometric alumina with a very low carbon concentration (<1 wt.%). The films do not diffract X-rays; they are dense and appear smooth but with a higher roughness than those obtained from vaporized pure ATI [19]. Detailed results on the microstructural and physicochemical characteristics of the films will be presented in a forthcoming paper.

4.1. Deposition in non-optimized configuration

The reactor configuration and operating conditions which were used for the deposition on flat substrates were applied to the deposition on the inner surface of the bottles. A first series of runs, with a generic name “Run A” was performed with a 15 mm distance between the nozzle and the bottle and with an inner nozzle diameter at its outlet of 2 mm. A schematic representation of the reactor for Run A is given in Fig. 2. Fig. 3 presents two photographs of the side and the external bottom of the coated bottle (Fig. 3a). The observed iridescences witness effective deposition and are acceptable for the targeted application. The lateral walls are transparent except at their lower part which is coated with a powdery white layer. In the bottom area near the central axis, the film is so thick that it has been delaminated. The experimental conversion rate of ATI, calculated as the mole number ratio between the deposited aluminum on the bottle (determined by weighing of the bottle before and after deposition) and the injected aluminum is 64%. Fig. 3b presents the experimentally determined alumina thickness profile

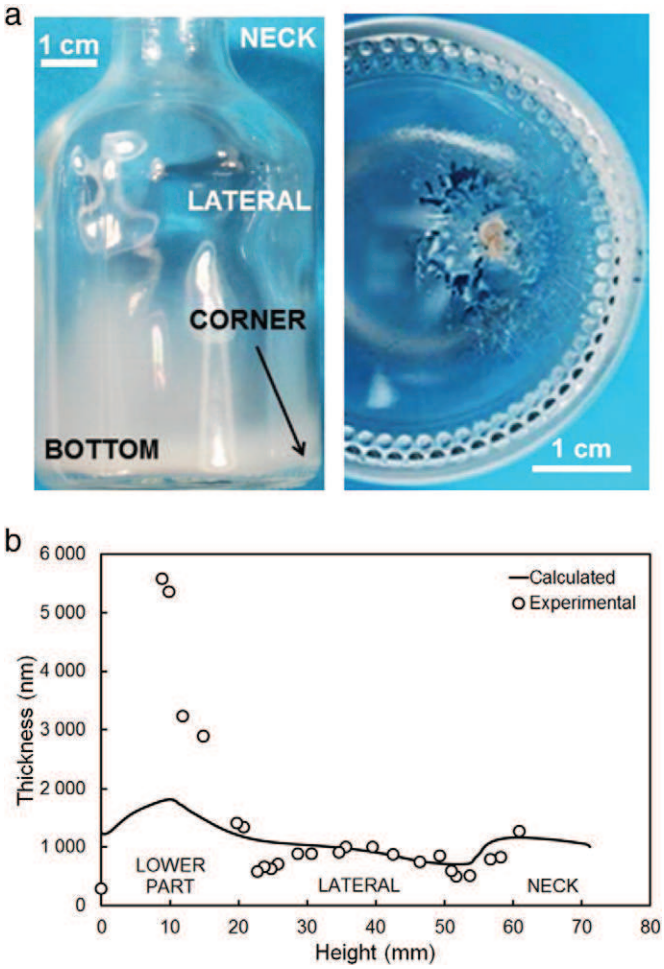

Fig. 3. Side and bottom view photographs of the coated bottle in Run A (a). Experimental (dots) and simulated (bold line) thickness profiles of a-Al_2O_3 along the height of the inner bottle walls (b).

(dots) after Run A along the internal lateral walls. The thickness on the lateral walls (height of bottle from 20 to 55 mm) ranges between 600 and 1000 nm. It will be reported in a forthcoming paper that despite a variation of ±200 nm, corresponding to a deviation of ±25% from the mean value of 800 nm, this thickness profile is acceptable, since the optical transparency, the adhesion and the hydrolytic resistance of the film meet the specifications. Nevertheless, two over-thicknesses are observed at the lower part (up to 5600 nm from 0 to 20 mm) and at the entrance (up to 1300 nm from 55 to 73 mm).

Fig. 4 shows cross-section SEM micrographs of the film for two different regions of the bottle. On the lateral walls and at the entrance, the film is dense and smooth in agreement with previous studies and with preliminary deposition on flat silicon substrates (Fig. 4b). The white layer at the lower part of the lateral walls presents a nodular microstructure composed of spherical particles aggregated on the film surface (Fig. 4a). The presence of white particles at the lower part can be correlated with the film delamination and the high thickness in this region. In this configuration, the process is not optimized to form conformal, adherent and transparent a-Al_2O_3 films.

4.2. Modeling deposition of Run A

The bold line in the diagram of Fig. 3b corresponds to the simulated thickness profile. It is almost uniform at the central part of the lateral walls with a mean value of 1000 nm. It presents two over-thicknesses, one at the lower part of the bottle and another at the neck walls, with

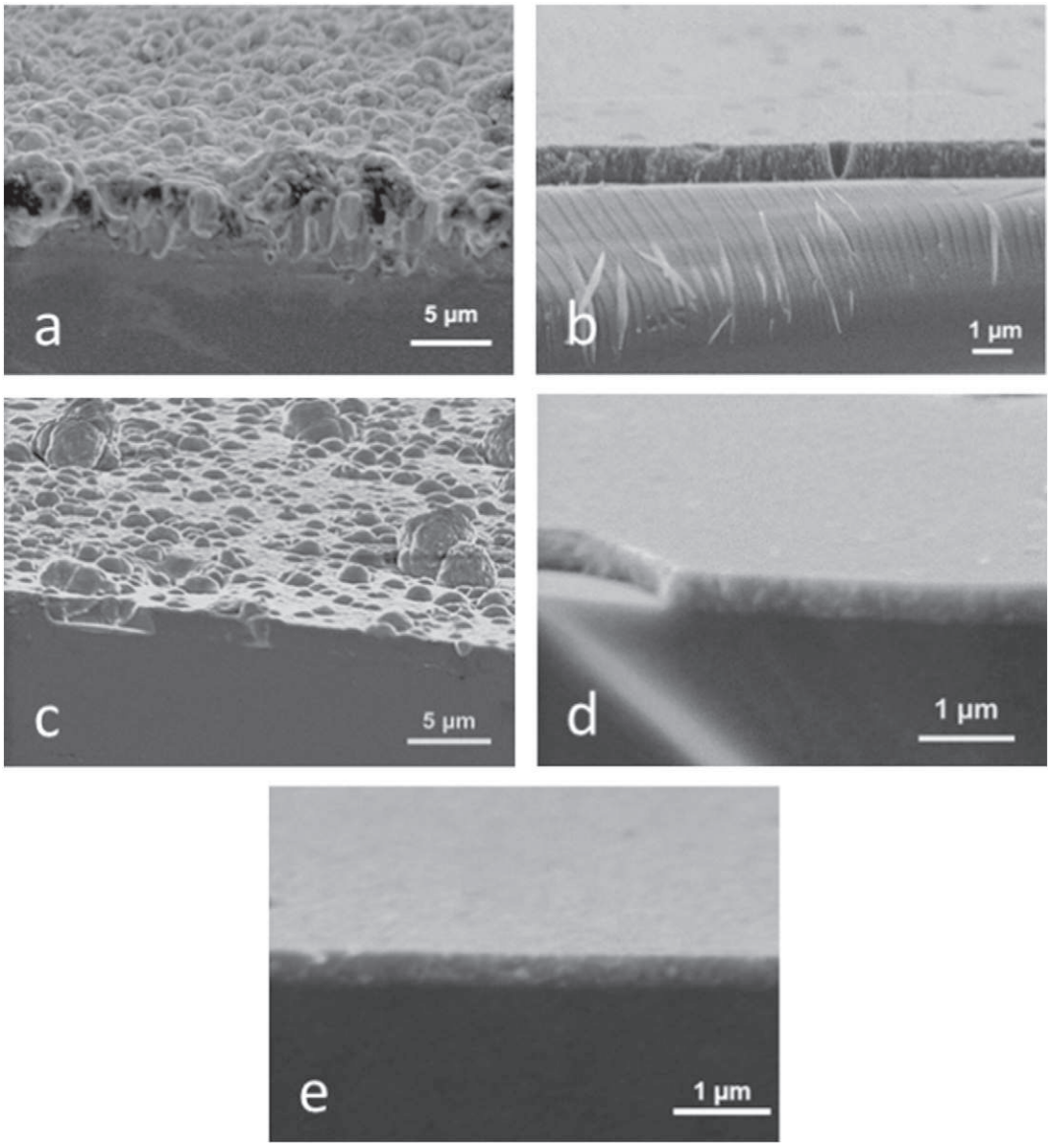

Fig. 4. SEM cross-section micrographs of a-Al_2O_3 films at the lower part (Run A: a, Run B: c) and the central part of the lateral walls (Run A: b, Run B: d, Run C: e).

maximum values of 1800 and 1200 nm, respectively. A good agreement between experimental results and simulation is observed at the entrance and on the lateral walls, namely in the regions where colorful iridescences are present and where the coating microstructure is dense and smooth. The model also correctly represents the high thickness on the neck walls. However it under-estimates the over-thickness of the white powdery stain at the lower part of the bottle. In this region, a different deposition mechanism probably exists which is not represented by the model, as explained below. The theoretical conversion rate of ATI calculated as the ratio of the ATI flow rate consumed on the inner walls of the bottle and the ATI flow rate at the reactor inlet is 53%. This calculated conversion rate of ATI is lower than the experimental one (64%) probably because deposition on the external walls of the bottle was not taken into account.

Figs. 5, 6 and 7 present the calculated gas velocity profiles, prevailing at the entire volume, at the lower part, and at the entrance of the bottle, respectively. The scales of velocities higher than 100, 150, and 400 m/s (Figs. 5, 6 and 7, respectively) existing along the axis are saturated for a better representation of the flows inside the bottle. The results reveal high gas velocity (ca. 470 m/s) at the nozzle outlet due to its narrow section. Gas flow with high axial velocity enters into the bottle as an impacting jet perpendicular to the bottom surface with high gradients and a sharp change of direction after hitting the bottom surface. Overall, gas velocities and velocity gradients inside the bottle are high, in particular at the bottom corner and at the entrance of the bottle, ranging between 0 and 410 m/s. Considering the size and the orientation of the velocity vectors in Figs. 6 and 7 it is concluded that, after hitting the bottom surface, the flow near the corner surface is disrupted by the inlet vertical flow, leading to a recirculation loop. In the same way, at the entrance, the outgoing flow hits the nozzle outlet, leading to its mixing with the inlet flow.

Fig. 8 presents the calculated ATI molar fraction at the entire volume of the bottle. It reveals that ca. 70% of the ATI initial concentration arrives at the inner lower part of lateral walls. However, the ATI molar fraction is not uniform, with values ranging from 0.6 10^{-3} to 1.2 10^{-3}. The high inlet flow rate impacting the central bottom surface is very concentrated in ATI and may lead to a thick, delaminated coating, as shown in Fig. 3b. Fig. 9 presents the calculated ratio in percentage of incoming ATI convective molar flow integrated on a given horizontal section of the bottle (or of the nozzle outlet) with regard to the ATI molar flow at the nozzle inlet. For Run A, the percentage is systematically higher than 100% and it increases with increasing the distance from

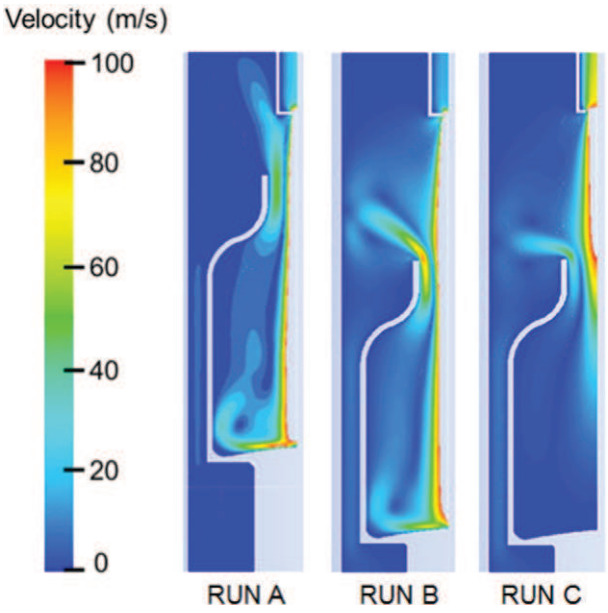

Fig. 5. Local gas velocity profiles in the reactor for Run A (left), Run B (center), and Run C (right). Velocities higher than 100 m/s existing along the axis are saturated for a better representation of the flow inside the bottle.

the entrance in the bottle. A value higher than 100% means that, at a given point the ATI molar flow is higher than that at the nozzle entrance. In steady state conditions this phenomenon is attributed to the gas flow recirculation which mixes the incoming and the outcoming gas flows at the bottom and between the bottle and the nozzle. This result is coherent with those illustrated in Figs. 6 and 7 on the profile of the local velocity vectors. Indeed, the very high precursor fluxes existing in the impacting jet and the increase of the residence time created by the recirculation phenomenon could create homogeneous reactions leading to gas phase nucleation, then to aggregation and sedimentation of particles falling down on the surface. This could explain the white powdery stain.

Along the lateral and the bottle neck walls, the kinetic law of the heterogeneous ATI decomposition successfully represents the film deposition. Especially, the over-thickness near the bottle neck due to the relatively high outlet flow rate and ATI concentration is well represented by the model. It is concluded that in the lateral and the bottle neck walls, conditions of flow and precursor supply are well suited for convenient deposition of alumina. The high precursor flux prevailing in the impacting jet and the recirculation phenomena favor homogeneous reactions, among ATI molecules and between them and by-product molecules from the outlet flow, like water vapor. Indeed, this reactor configuration generates high precursor molar fraction and important convective flow, which can increase the probability of impact among reactive molecules favoring homogeneous reactions. This situation results in gas phase nucleation, followed by aggregation and sedimentation of particles on the surface.

4.3. First improvement: influence of the distance between nozzle and bottle

On the basis of the previous results, the aim of the depositions in Run B configuration was to decrease the precursor supply inside the bottle and the velocity of the impacting jet in order to limit the gas recirculation, then increasing the mass transport limited behavior of the process. The reactor configuration was accordingly modified by increasing the distance between the nozzle and the bottle from 15 mm to 40 mm. This modification also led to the translation of the bottle relatively to the heating SS tube. While maintaining a temperature of 480 °C on the external bottom wall, this shift generated a new thermal profile, presented in Fig. 2 where in particular temperatures on the neck walls are higher than those in Run A. A schematic representation of the reactor for Run B is given in Fig. 2. The calculated flow profile is almost similar to that of Run A (Fig. 5): the inlet flow is mainly axial with high values, then impacts the bottom surface and finally slips through the neck walls. The gas velocity at the nozzle outlet is slightly increased to 530 m/s in comparison with Run A. This can be explained by the different thermal profile which decreases the gas density for this run. However, gas velocities inside the bottle are lower, ranging between 0 and 300 m/s, because the distance between the nozzle and the bottle is higher. Figs. 6 and 7 present the velocity vectors at the bottle bottom and at the entrance respectively. It appears that the phenomena of impacting jet and of gas recirculation near the bottom still exist. However, Fig. 7 shows that the flow exiting from the bottle is less disrupted by the inlet gas flow than in the configuration of Run A. The ATI supply from the nozzle outlet is lower than for Run A because of a higher consumption of ATI into the nozzle due to its higher temperature in this configuration (Fig. 8). The comparison of ATI molar fractions between Run A and Run B emphasizes the considerable decrease of precursor supply inside the bottle. Fig. 8 shows that supply of ATI in Run B is lower but more uniform along the internal walls of the bottle. Fig. 9 shows that the ratio at the bottle entrance is lower than 100% and that it moderately increases inside the bottle for heights between 0 and 20 mm. These results reveal decrease of gas recirculation, which is more significant at the entrance of the bottle.

Bottles processed in conditions Run B present marked iridescences indicating efficient deposition on the lateral and neck walls. Nevertheless, white powdery stain is still present at the bottom corner. The film is also slightly delaminated in this zone but flaking is less important than for Run A. Microstructures at the lower part (Fig. 4c) and at the central part of the lateral walls (Fig. 4d) are similar to the ones obtained from Run A; i.e. a dense layer on the lateral walls, and spherical particles

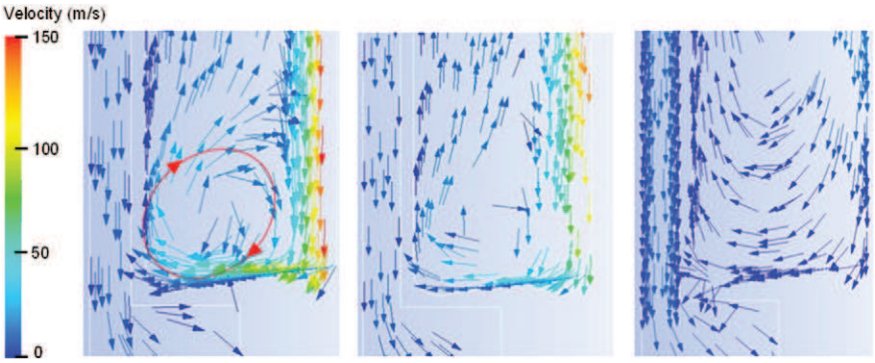

Fig. 6. Velocity vectors at the bottom of the bottle for Run A (left), Run B (center) and Run C (right). Velocities higher than 150 m/s existing along the axis are saturated for a better representation of the flow inside the bottle.

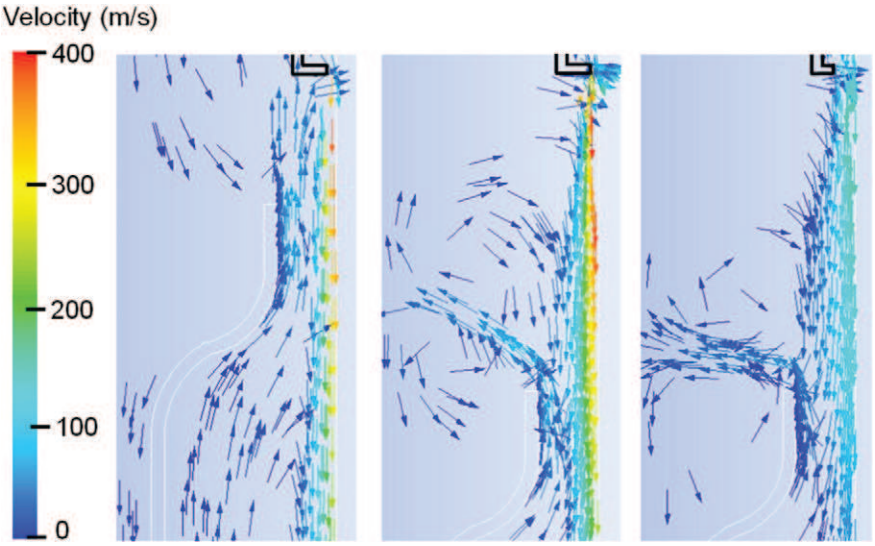

Fig. 7. Velocity vectors at the entrance of the bottle for Run A (left), Run B (center) and Run C (right). Velocities higher than 400 m/s existing along the axis are saturated for a better representation of the flow inside the bottle.

at the bottom corner. It is concluded that the gas velocities and the ATI supply, as presented in Figs. 5 to 8, are not low enough to avoid homogeneous reactions. The theoretical conversion rate of ATI inside the bottle is 34%. The experimental conversion rate of ATI on the inner and outer walls is 40%; i.e. lower than for Run A. This can be correlated with the lower ATI supply inside the bottle due to high consumption in the entrance tube.

Fig. 10 presents the experimental and calculated thickness profiles obtained in the conditions of Run B. Thickness at the neck and lateral walls of the bottle is uniform, while a slight overgrowth is observed at the entrance. This result is reliably reproduced by the calculated thickness profile, which predicts an over-thickness at the entrance attaining 900 nm and an almost flat profile at the lateral walls with a mean thickness of 400 nm. Convective and diffusive conditions in these regions with relatively low velocity gradients, low gas recirculation and low ATI concentrations are convenient for the conformal deposition of alumina (with limited undesirable reactions), that the model successfully represents. At the lower part of the bottle, the experimentally determined thickness attains a maximum value of 2100 nm, corresponding to the white powdery layer, as previously observed for coatings processed in Run A. The model does not catch this overgrowth. Despite the fact that thickness is more uniform than that of Run A (Fig. 3b), the reactor configuration and/or processing conditions need to be further improved to avoid the white powdered overgrowth at the bottom part of the bottle.

4.4. Second improvement: influence of the nozzle outlet section

Minimization of the impacting jet and hence elimination of the significant overgrowth at the bottom lower part of the bottle can be achieved by decreasing the velocity of the input gas and/or by increasing the deposition pressure. Technical specifications of the DLI equipment do not allow the former. Increasing the deposition pressure is not our priority since the appropriate kinetic model is not available, thus preventing us actually from process simulation in these conditions. Velocity decrease was finally achieved by increasing the inner diameter of the outlet nozzle section from 2 mm to 5 mm. In this configuration, named Run C, the distance between bottle and nozzle was kept to 40 mm.

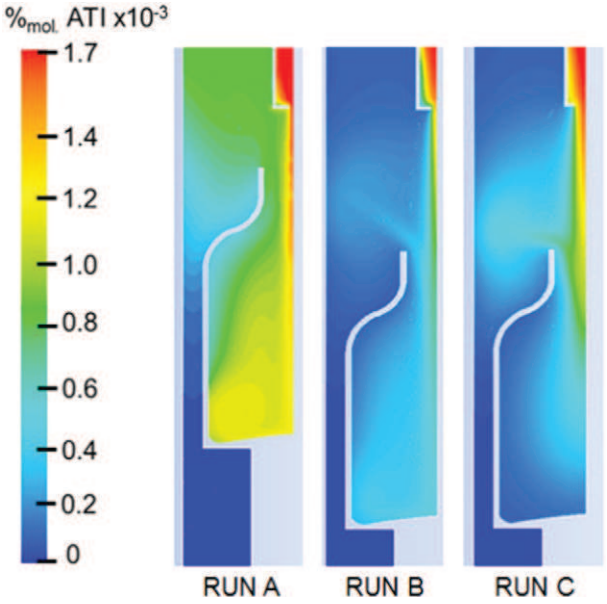

Fig. 8. Local ATI molar fraction profiles in the reactor for Run A (left), Run B (center) and Run C (right).

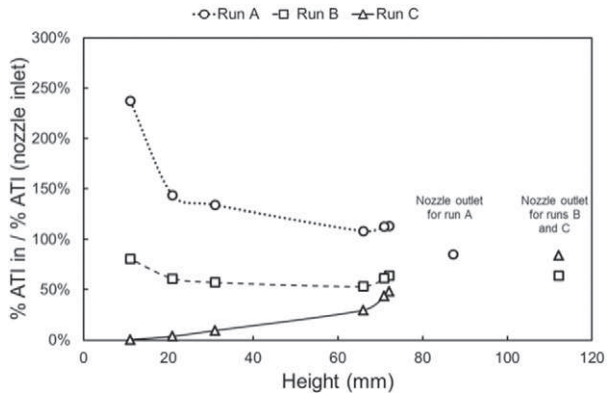

Fig. 9. Calculated inlet ATI flow reported to ATI flow at the nozzle inlet for Run A, Run B, and Run C, at the nozzle inlet and at several horizontal sections of the bottle.

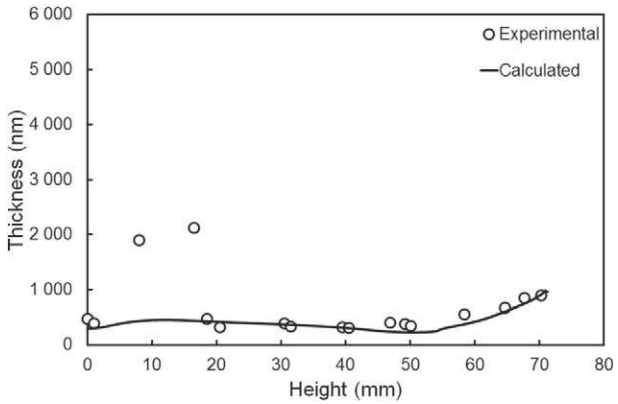

Fig. 10. Experimental (dots) and simulated (bold line) thickness profiles of a-Al_2O_3 film along the height of the inner bottle wall for Run B.

A schematic representation of the reactor for Run C is given in Fig. 2. Figs. 5 to 8 show the corresponding calculated local profiles of gas velocity and ATI molar fraction. The velocity field is different from those of Run A and Run B. The inlet flow is still mainly axial near the central axis; the maximum gas velocity at the nozzle outlet is 154 m/s whereas velocities inside the bottle are between 0 and 100 m/s. These results correspond to lower flow and velocity values than in previous runs. Figs. 6 and 7 show the gas velocity vectors at the bottom and near the neck walls respectively. The gas flow reaches the inner lower part of the lateral surface smoothly with moderate velocity gradients, eliminating the impacting jet and gas recirculation phenomena. The outlet flow toughly slips on the neck walls with vectors parallel to the surface and going out from the bottle with negligible interaction with the inlet flow.

The local profile of ATI concentration in Run C is also different compared with Run A and Run B due to the lower precursor supply to the inner volume of bottle. Also, more ATI is consumed in the nozzle for Run B (Fig. 8) because of a slightly higher pressure, higher residence time and higher temperature in the inner corner of the nozzle outlet, working as a diaphragm. On the other hand, in conditions of Run C, the ATI concentration close to the inner lateral walls is more uniform but less ATI molecules enter the bottle because of lower convective transport. Hence, in Run C, the ratio between the ATI molecules entering inside the bottle and those consumed is lower than in Run B because of the overall lower ATI supply. Fig. 9 shows that in Run C the inlet ATI molar fraction at the bottle entrance is lower than that at the nozzle inlet (abscissa 73 mm and 113 mm, respectively). Further in the bottle, the inlet ATI molar fraction slightly decreases from the neck to the bottom. These two results confirm the suppression of gas recirculation phenomena in Run C.

The calculated coating thickness profile is plotted in Fig. 11. From the bottom corner to the bottle shoulder (from 0 to 55 mm), the calculated

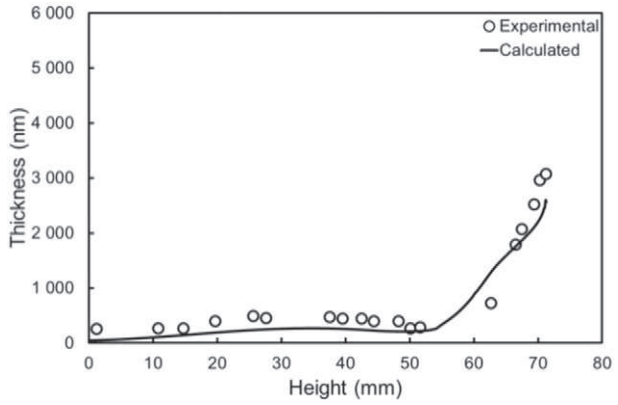

Fig. 11. Experimental (dots) and simulated (bold line) thickness profiles of a-Al_2O_3 film along the height of the inner bottle wall for Run C.

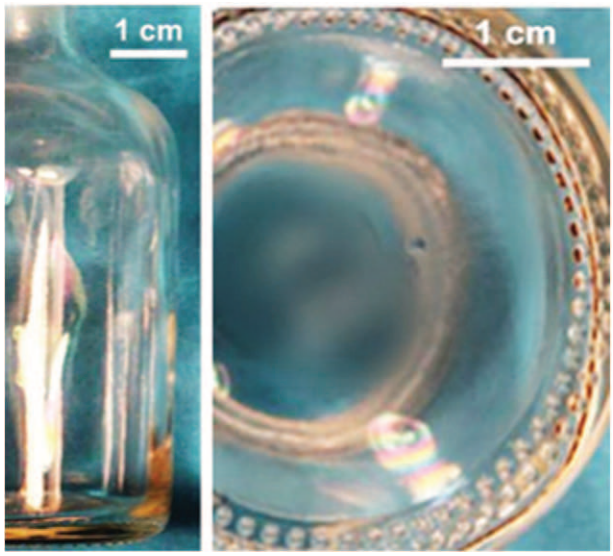

Fig. 12. Photographs of the coated bottle in Run C: side (left) and bottom (right) views.

thickness is almost uniform ranging between 250 and 450 nm and is lower than for Runs A and B (Figs. 3b and 10). The simulation predicts once again the over-thickness on the neck walls which exceeds 3000 nm.

The two photographs of Fig. 12 present a bottle processed in conditions of Run C. Bottle walls show distinct iridescences witnessing effective deposition (Fig. 12, left), while there is an over-thickness associated with a white powdery layer (Fig. 12, right). The alumina film presents a dense microstructure all over the glass surface, as presented in Fig. 4e. The experimental conversion rate of ATI in the bottle is 29% while the theoretical one which only takes into account the deposition on the inner walls is 19%.

The experimentally determined thickness profile of the film is plotted in Fig. 11. There is an excellent agreement between calculated and experimental thickness profiles along the entire height of the bottle. On the lateral walls, the calculated and experimental profiles are slightly curved, which can be related to the experimental parabolic thermal profile (Fig. 2) and also to the ATI molar fraction field in this area (Fig. 8). Film thickness at the entrance is significant due to higher local temperatures, high convective flow slipping the walls and ATI molar fraction. This film is probably deposited through the same mechanism as the one occurring on the lateral walls, well described by the kinetic law. The new reactor configuration with the nozzle far enough from the bottle and the large diameter of the nozzle outlet allows generating relatively low velocity gradients inside the bottle, avoiding gas recirculation and thus resulting in well suited gas flow for the deposition of alumina with the targeted characteristics. The precursor supply is also lower which contributes to the decrease of the probability of homogeneous nucleation reactions.

5. Conclusions

Coating the inner walls of a bottle requires a more elaborated approach than depositing on flat substrates because of the complex geometry formed by a cavity with a unique, narrow inlet/outlet orifice. The present work emphasizes the interest to combine experiments and numerical modeling to optimize a complex MOCVD process such as the one of coating the inner walls of a bottle. Direct Liquid Injection MOCVD of a-Al_2O_3 films was performed from ATI at 666 Pa in a vertical hot-wall reactor in the mass-transport limited regime. First experiments yielded dense a-Al_2O_3 films on the lateral walls and a white powdery stain composed of sub-micrometric particles at the bottom corner forming a local over-thick coating. A reactor model using the CFD code

Fluent and a kinetic law of the apparent heterogeneous reaction of ATI was developed. A satisfactory agreement between experimental and calculated film thickness profiles was found on the lateral wall. The simulation revealed that the deposited over-thicknesses come from high convective flow, gas recirculation and high ATI supply, which can be locally responsible for the homogeneous nucleation of ATI. Then, the model was used for process improvement, by providing trends to modify the reactor configuration in order to decrease the gas flow impacting the bottle bottom, the gas recirculation and the ATI supply. Increasing the distance between the nozzle and the bottle and mainly increasing the diameter of the nozzle outlet allowed obtaining well suited conditions for the deposition of transparent amorphous alumina coatings.

Acknowledgments

We are indebted to Djar Oquab and Yannick Thebault, both at CIRIMAT for help with SEM operation, and to Philippe de Parseval, UMS Castaing, for the EPMA characterizations.

References

[1] C.R. Kleijn, R. Dorsman, K.J. Kuijlaars, M. Okkerse, H. van Santen, Multi-scale modeling of chemical vapor deposition processes for thin film technology, J. Cryst. Growth 303 (2007) 362–380.
[2] M.E. Coltrin, R.J. Kee, J.A. Miller, A mathematical-model of the coupled fluid-mechanics and chemical-kinetics in a chemical vapor-deposition reactor, J. Electrochem. Soc. 131 (1984) 425–434.
[3] M.E. Coltrin, R.J. Kee, J.A. Miller, A mathematical-model of silicon chemical vapor-deposition — further refinements and the effects of thermal-diffusion, J. Electrochem. Soc. 133 (1986) 1206–1213.
[4] C.R. Kleijn, A mathematical-model of the hydrodynamics and gas-phase reactions in silicon LPCVD in a single-wafer reactor, J. Electrochem. Soc. 138 (1991) 2190–2200.
[5] Y.K. Chae, Y. Egashira, Y. Shimogaki, K. Sugawara, H. Komiyama, Chemical vapor deposition reactor design using small-scale diagnostic experiments combined with computational fluid dynamics simulations, J. Electrochem. Soc. 146 (1999) 1780–1788.
[6] C.R. Kleijn, On the modeling of transport phenomena in chemical vapor-deposition and its use in reactor design and process optimization, Thin Solid Films 206 (1991) 47–53.
[7] T.C. Xenidou, A.G. Boudouvis, N.C. Markatos, D. Samelor, F. Senocq, N. PrudHomme, C. Vahlas, An experimental and computational analysis of a MOCVD process for the growth of Al films using DMEAA, Surf. Coat. Technol. 201 (2007) 8868–8872.
[8] T.C. Xenidou, N. Prud'homme, C. Vahlas, N.C. Markatos, A.G. Boudouvis, Reaction and transport interplay in Al MOCVD investigated through experiments and computational fluid dynamic analysis, J. Electrochem. Soc. 157 (2010) D633–D641.
[9] H. Vergnes, D. Samelor, A.N. Gleizes, C. Vahlas, B. Caussat, Local kinetic modeling of aluminum oxide metal-organic CVD from aluminum tri-isopropoxide, Chem. Vap. Depos. 17 (2011) 181–185.
[10] R. Hofman, R.W.J. Morssinkhof, T. Fransen, J.G.F. Westheim, P.J. Gellings, Thin alumina and silica films by chemical vapor deposition (CVD), Mater. Manuf. Process. 8 (1993) 315–329.
[11] M. Kawase, Y. Ikuta, T. Tago, T. Masuda, K. Hashimoto, Modeling of a thermal-gradient chemical-vapor infiltration process for production of silicon-carbide whisker alumina composite, Chem. Eng. Sci. 49 (1994) 4861–4870.
[12] N. Boutroy, Y. Pernel, J.M. Rius, F. Auger, H.J. von Bardeleben, J.L. Cantin, F. Abel, A. Zeinert, C. Casiraghi, A.C. Ferrari, J. Robertson, Hydrogenated amorphous carbon film coating of PET bottles for gas diffusion barriers, Diam. Relat. Mater. 15 (2006) 921–927.
[13] M. Deilmann, H. Halfmann, S. Steves, N. Bibinov, P. Awakowicz, Silicon oxide permeation barrier coating and plasma sterilization of PET bottles and foils, Plasma Process. Polym. 6 (2009) S695–S699.
[14] M. Ikeyama, S. Miyagawa, Y. Miyagawa, Y. Hayakawa, T. Miyajima, DLC coatings on inner walls of PET bottles by a simplified PBII technique, Surf. Coat. Technol. 201 (2007) 8112–8115.
[15] W. Marten, CVD for Internal Coating Of Hollow Articles With Barrier Film US5972436, 1997.
[16] J.-M. Rius, Gas Feed Installation for Machines Depositing a Barrier Layer on Containers, 2006. (WO2007063015).
[17] J.-M. Rius, Apparatus for Depositing a Coating on the Internal Surface of a Container EP1881088, 2007.
[18] A. Shirakura, M. Nakaya, Y. Koga, H. Kodama, T. Hasebe, T. Suzuki, Diamond-like carbon films for PET bottles and medical applications, Thin Solid Films 494 (2006) 84–91.
[19] Y. Balcaen, N. Radutoiu, J. Alexis, J.D. Beguin, L. Lacroix, D. Samelor, C. Vahlas, Mechanical and barrier properties of MOCVD processed alumina coatings on Ti6Al4V titanium alloy, Surf. Coat. Technol. 206 (2011) 1684–1690.
[20] D. Samelor, A.M. Lazar, M. Aufray, C. Tendero, L. Lacroix, J.D. Beguin, B. Caussat, H. Vergnes, J. Alexis, D. Poquillon, N. Pebere, A. Gleizes, C. Vahlas, Amorphous alumina coatings: processing, structure and remarkable barrier properties, J. Nanosci. Nanotechnol. 11 (2011) 8387–8391.
[21] P.L. Etchepare, H. Vergnes, D. Samélor, D. Sadowski, C. Brasme, B. Caussat, C. Vahlas, Amorphous alumina coatings on glass bottles using direct liquid injection MOCVD for packaging applications, Adv. Sci. Technol. 91 (2014) 117–122.
[22] A.M. Lazar, W.P. Yespica, S. Marcelin, N. Pebere, D. Samelor, C. Tendero, C. Vahlas, Corrosion protection of 304L stainless steel by chemical vapor deposited alumina coatings, Corros. Sci. 81 (2014) 125–131.
[23] P. Nayar, A. Khanna, D. Kabiraj, S.R. Abhilash, B.D. Beake, Y. Losset, B. Chen, Structural, optical and mechanical properties of amorphous and crystalline alumina thin films, Thin Solid Films 568 (2014) 19–24.
[24] M. Klause, U. Rothhaar, M. Bicker, W. Ohling, Dissolution of thin SiO_2-coatings — characterization and evaluation, J. Non-Cryst. Solids 356 (2010) 141–146.
[25] M.M. Sovar, D. Samélor, A.N. Gleizes, C. Vahlas, Aluminium tri-iso-propoxide: shelf life, transport properties, and decomposition kinetics for the low temperature processing of aluminium oxide-based coatings, Surf. Coat. Technol. 201 (2007) 9159–9162.
[26] A.N. Gleizes, C. Vahlas, M.M. Sovar, D. Samelor, M.C. Lafont, CVD-fabricated aluminum oxide coatings from aluminum tri-iso-propoxide: correlation between processing conditions and composition, Chem. Vap. Depos. 13 (2007) 23–29.
[27] S. Blittersdorf, N. Bahlawane, K. Kohse-Hoinghaus, B. Atakan, J. Muller, CVD of Al_2O_3 thin films using aluminum tri-isopropoxide, Chem. Vap. Depos. 9 (2003) 194–198.
[28] V. Sarou-Kanian, A.N. Gleizes, P. Florian, D. Samelor, D. Massiot, C. Vahlas, Temperature-dependent 4-, 5- and 6-fold coordination of aluminum in MOCVD-grown amorphous alumina films: a very high field Al-27-NMR study, J. Phys. Chem. C 117 (2013) 21965–21971.
[29] R.W.J. Morssinkhof, The deposition of thin alumina films on steels by MOCVD, Synthesis, Characterization and Protective Properties Against High Temperature Corrosion, University of Twente, 1991.
[30] A.N. Gleizes, M.-M. Sovar, D. Samélor, C. Vahlas, Low temperature MOCVD-processed alumina coatings, Adv. Sci. Technol. 45 (2006) 1184–1193.
[31] S.K. Soni, D. Samelor, B.W. Sheldon, C. Vahlas, A.N. Gleizes, Residual stress mechanisms in aluminium oxide films grown by MOCVD, ECS Trans. 25 (2009) 1309–1315.
[32] S. Krumdieck, S. Davies, C.M. Bishop, T. Kemmitt, J.V. Kennedy, Al_2O_3 coatings on stainless steel using pulsed-pressure MOCVD, Surf. Coat. Technol. 230 (2013) 208–212.
[33] D. Samélor, M. Aufray, L. Lacroix, Y. Balcaen, J. Alexis, H. Vergnes, D. Poquillon, J.D. Beguin, N. Pébère, S. Marcelin, B. Caussat, C. Vahlas, Mechanical and surface properties of chemical vapour deposited protective aluminium oxide films on TA6V alloy, Adv. Sci. Technol. 66 (2010) 66–73.
[34] C. Vahlas, B. Caussat, W.-L. Gladfelter, F. Senocq, E.J. Gladfelter, Liquid and solid precursor delivery systems in gas phase processes, Recent Patents on Complex Metallic Alloys 8 (2) (2015) 91–108.
[35] R.B. Bird, W.E. Stewart, E.N. Lightfoot, Transport Phenomena, second edition John Wiley & Sons, 2007.